



Sea-urchin-structure $\text{g-C}_3\text{N}_4$ with narrow bandgap (~ 2.0 eV) for efficient overall water splitting under visible light irradiation



Yunxiong Zeng^{a,1}, Hao Li^{c,1}, Jinming Luo^{b,*}, Jili Yuan^a, Longlu Wang^a, Chengbin Liu^a, Yingchun Xia^a, Meijun Liu^a, Shenglian Luo^a, Tao Cai^a, Su Liu^b, John C. Crittenden^b

^a State Key Laboratory of Chemo/Biosensing and Chemometrics, Hunan University, Changsha 410082, PR China

^b Brook Byers Institute for Sustainable Systems and School of Civil and Environmental Engineering, Georgia Institute of Technology, 828 West Peachtree Street, Atlanta, Georgia 30332, United States

^c Department of Chemistry and Institute for Computational and Engineering Sciences, The University of Texas at Austin, 105 E. 24th Street, Stop A5300 Austin, Texas 78712, United States

ARTICLE INFO

Keywords:

$\text{g-C}_3\text{N}_4$
Hierarchical sea-urchin-structure
~2.0 eV Bandgap
Water splitting
Visible light photocatalysts

ABSTRACT

A broad bandgap and detrimental recombination of photoexcited h^+e^- pairs are fatal deficiencies for using the $\text{g-C}_3\text{N}_4$ visible light water splitting. Herein, a sea-urchin-structure $\text{g-C}_3\text{N}_4$ (CNSC) with ~ 2.0 eV bandgap was prepared using a hydrothermal strategy. It is important to note that CNSC can efficiently suppress h^+e^- pair recombination and has a narrow bandgap which can utilize more visible light. Conventional $\text{g-C}_3\text{N}_4$ has a ~ 2.7 eV bandgap and valence band (VB) potential of $+1.83$ V vs. NHE but the VB of CNSC is $+1.55$ V. As a result, CNSC does not create H_2O_2 , which can passivate $\text{g-C}_3\text{N}_4$. Density functional theory (DFT) confirms that $\text{C}\equiv\text{N}$, $\text{C}=\text{O}$, and $-\text{OH}$ groups in the CNSC shift the d-band centre of Pt closer to Fermi level, leading to better stabilization of adsorbate and higher catalytic performance. Photo-depositing Pt on the CNSC, 3 wt% Pt/CNSC produces H_2 and O_2 evolution rate (HER and OER) of 41.5 and $20.3 \mu\text{mol g}^{-1} \text{h}^{-1}$ (apparent quantum efficiency: 0.43% at 420 ± 10 nm), respectively, 30 times greater than HER of 2 wt% Pt/bulk $\text{g-C}_3\text{N}_4$ in overall water splitting under visible-light ($\lambda \geq 420$ nm). This work provides an innovative approach to construct hierarchical nanostructure $\text{g-C}_3\text{N}_4$ with narrow bandgap and paves the pathway for development of water splitting photocatalysts.

1. Introduction

Water splitting is a sustainable approach to replace fossil fuels and reduce environment pollution that is associated with energy production. [1–3] From a practical point of view [4–6], high-efficiency and low-cost visible light photocatalysts are very desirable. [7–10] $\text{G-C}_3\text{N}_4$ as a metal-free photocatalyst is attracting tremendous attention due to adjustable electronic structures and optical properties. [11–14] The broad bandgap (around 2.7 eV) limits its visible light utilization and photoexcited h^+e^- pairs recombination is a fatal deficiency for $\text{g-C}_3\text{N}_4$ photocatalysts [15–17]. Until now, most researches were focused on heterojunction fabrication, large bandgap and high h^+e^- pairs recombination problems of $\text{g-C}_3\text{N}_4$, although, these issues had not been resolved. [18–23]

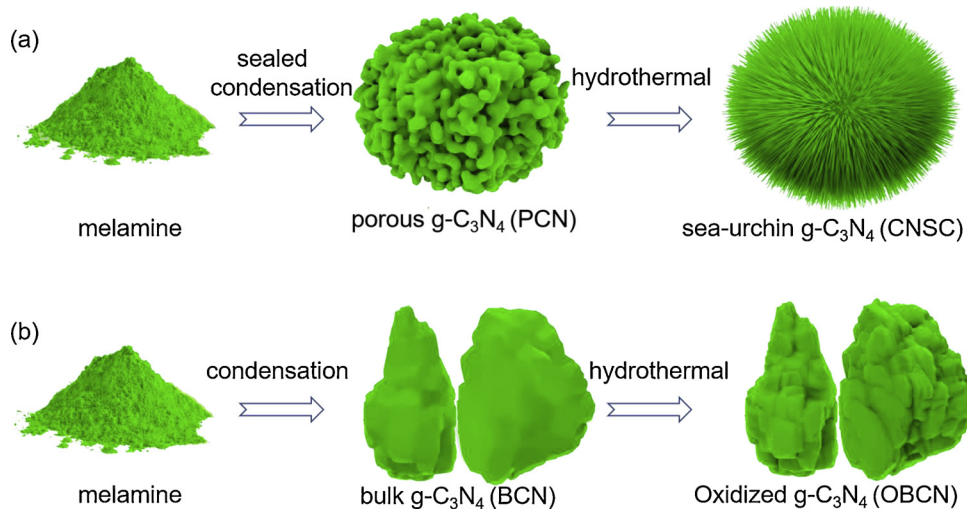
The $\text{g-C}_3\text{N}_4$ photocatalyst with a ~ 2.0 eV narrow bandgap makes better use of the solar spectrum for water splitting. The $\text{g-C}_3\text{N}_4$

photocatalyst with ca. 2.0 eV bandgap was prepared by: (1) chemical etching $\text{g-C}_3\text{N}_4$ in a H_2 atmosphere, [24] (2) sodium borohydride etching of bulk $\text{g-C}_3\text{N}_4$ at $150\text{--}350$ °C, [25] and (3) calcining bulk $\text{g-C}_3\text{N}_4$ at $510\text{--}620$ °C under Ar atmosphere. [26,27] Typical fabrications procedure include a multi-step process with the assistance of alkali or harsh reduction gas [28]. One problem is that the produced $\text{g-C}_3\text{N}_4$ suffers from structure agglomeration in most cases. [26–29] Meanwhile, ultrafast h^+e^- pairs recombination (typically on $10^{-12}\text{--}10^{-9}$ s) is considered to be the most crucial factor for poor performance. [27–30] To avoid this, heterojunctions using additional semiconductors induce interfacial electric field via energy band matching to enable charge directed migration [31,32]. Such heterojunction configurations are not only governed by the electronic crystal structures and surface/interface properties, but also significantly affected by energy band bending due to block carrier migration. In contrast, the hierarchical nanostructure is highly favorable for photoinduced h^+e^- pairs separation without been

* Corresponding author.

E-mail address: jinming.luo@ce.gatech.edu (J. Luo).

¹ These authors contributed equally to this work.



Scheme 1. Formation mechanism of (a) hierarchical CNSC using sealed condensation approach and (b) BCN using traditional condensation route.

affecting by additional semiconductors. [33–35] Therefore, developing $\text{g-C}_3\text{N}_4$ photocatalyst with narrow bandgap, rational band structure and unique nanostructure with large specific area is urgently desired to boost catalytic activity.

Herein, we prepared a sea-urchin nanostructured $\text{g-C}_3\text{N}_4$ with a 2.07 eV narrow bandgap using a facile hydrothermal approach (Scheme 1a). First, the porous $\text{g-C}_3\text{N}_4$ (PCN) was synthesized under sealed condensation. [36–38] Meantime, the NH_3 released not only helps the formation of porous nanostructures but also breaks heptazine ring to form nitrogen vacancies. [16] Next, the CNSC was prepared through hydrothermal etching the PCN. Distinctive from a traditional poor sealed condensation (Scheme 1b), bulk $\text{g-C}_3\text{N}_4$ (BCN) is oxidized into oxidizing-state bulky $\text{g-C}_3\text{N}_4$ (OBCN). [39,40] To the best of our knowledge, this is the first report on a one-step hierarchical $\text{g-C}_3\text{N}_4$ preparation with narrow bandgap (ca. 1.6 eV) and nitrogen vacancies using a bottom-to-up technique. We also found that the photocatalytic performance can be significantly enhanced by photo-reducing 3 wt% Pt onto CNSC. The HER and OER were 41.5 and $20.3 \mu\text{mol g}^{-1} \text{h}^{-1}$ for overall water splitting, respectively. And the HER for 3 wt% Pt/CNSC was 30 times higher than HER for 2 wt% Pt/BCN for water splitting under visible light ($\lambda \geq 420 \text{ nm}$).

2. Experimental section

2.1. Chemicals

Reagent grade chemicals were purchased from Sinopharm Chemical Reagent Co. Ltd and used without further purification. Ultrapure water was used in the whole experiment process (Millipore-Q Century, 18.2 $\text{M}\Omega \text{ cm}$).

2.2. Synthesis of bulk $\text{g-C}_3\text{N}_4$

Melamine powder ($\text{C}_3\text{H}_6\text{N}_6$, Mr = 126.12, 10.0 g) was put in a crucible with a lid (aluminum-nickel alloy, diameter of the mouth: 6.0 cm, diameter of bottom: 5.0 cm) and heated to 550 °C in a silica oxide tube furnace (Hefei Kejing Co., Ltd., interior diameter: 12 cm) at a heating rate of 2.5 °C/min under N_2 flow (99.999%, 50 mL/min). After keeping the sample for 4 h at 550 °C, it was cooled naturally to room temperature. The resulting sample was a light yellow and very hard block solid (ca. 3.5 g, yield: 35%) and named bulk $\text{g-C}_3\text{N}_4$ (BCN).

2.3. Oxidized bulk $\text{g-C}_3\text{N}_4$ sample

The BCN (0.23 g) was mixed with 60 mL distilled water, put into a

80-mL closed stainless steel pressure vessel (autoclave) with a Teflon inner liner and heated at 180 °C for 6 h. After allowing it to cool to room temperature, the mixture was centrifugalized at 4000 rpm (533 g) for 15 min. to remove any remaining suspended particles. Finally, the solid was dried at 60 °C overnight under a vacuum and named oxidized bulk $\text{g-C}_3\text{N}_4$ (OBCN, 0.12 g).

2.4. Porous $\text{g-C}_3\text{N}_4$ synthesis

Melamine powder ($\text{C}_3\text{H}_6\text{N}_6$, Mr = 126.12, 10.0 g) was put into a crucible (aluminum-nickel alloy, diameter of the mouth: 6.0 cm, diameter of bottom: 5.0 cm), next, sealed the crucible mouth with 2-layer silver papers (namely aluminum foil, a thickness of 10.0 μm), enwound the aluminum foil with 2 round stainless steel wires (diameter: 1.1 mm) and highly tightened the end of the steel wires with iron tong as much strength as possible. Then, sealed the crucible mouth again with 2-layer silver papers following by tightened with stainless steel wires, until repeating this procedure six times. Noted, the sealing crucible mouth with steel wires was key important to obtain solid sealed condition for melamine condensation. Finally, the well sealed crucible was put into silica oxide tube furnace (Hefei Kejing Co., Ltd., interior diameter: 12 cm) and heated to 550 °C at a heating rate of 2.5 °C/min under N_2 flow (99.999%, 50 mL/min), and kept for 4 h at 550 °C to obtain dark yellow porous block solid and powder mixture (ca. 3.8 g, yield: 38%). Noted, dark yellow and loose $\text{g-C}_3\text{N}_4$ powder (PCN, ca. 1.7 g, yield: 17%) was obtained after remove the porous hard solid.

2.5. Sea-urchin-structure $\text{g-C}_3\text{N}_4$ synthesis

The synthesized PCN powder (0.23 g) was put into 60 mL distilled water and stirred overnight. Next, the suspension was transferred to an 80-mL stainless steel pressure vessel (autoclave) with a Teflon inner liner and heated in an oven at 180 °C for 6 h. After cooling to room temperature, the mixture was centrifugalized at 4000 rpm (533 g) for 15 min. to remove any remaining suspended particles. Finally, the particles were dried at 60 °C overnight under vacuum to obtain sea-urchin-like $\text{g-C}_3\text{N}_4$ (CNSC, 0.10 g).

2.6. NH_3 emission rate during melamine condensation

As for NH_3 emission rate during melamine condensation to PCN and BCN, respectively, we quantified it by the acid-base back titration method (details seen in Supplementary Material). Briefly, NH_3 gradually went into the bottle and was absorbed by HCl solution. Next, used standard NaOH solution to titrate residual HCl solution with pH stick as

an indicator. Finally, NH_3 amount was calculated and converted into volume by ideal gas formula, thus, volume was divided by time to calculate NH_3 release rate (details seen in Supplementary Material).

2.7. Characterization

The morphologies and composition of samples were characterized by scanning electron microscopy (SEM) (Hitachi, S-4800), transmission electron microscopy (TEM) (JEOL, JEM-2100 F), powder X-ray diffraction (XRD) with Cu-K α radiation (Rigaku, Smartlab), Fourier transform infrared (FT-IR) spectra (Thermo Fisher Scientific), organic elemental analysis (OEA) and X-ray photoelectron spectroscopy (XPS) with Al-K α radiation (K-Alpha 1063, Thermo Fisher Scientific). The chemical element compositions were analyzed by the EDS mapping images captured on a Tecnai G2 F20 S-TWIN atomic resolution analytical microscope. The specific surface area was determined by the Brunauer-Emmett-Teller (BET) method with N_2 adsorption at 77 K (BELSORP-mini II). The UV-vis diffuse reflectance spectra (DRS) was recorded on Agilent, Cary 300 spectrophotometer. The photoluminescence (PL) spectra was recorded with Hitachi F-7000 fluorescence spectrophotometer. Electron spin resonance (ESR) was measured by a JES FA200 (JEOL) spectrometer at room temperature.

2.8. Photoelectrochemical measurement

The photocurrent, Mott-Schottky curve and Nyquist plot without bias potential were determined with a CHI 660C electrochemical analyzer (CHI Inc., USA) in 0.5 M Na_2SO_4 aqueous solution with a three-electrode configuration: (1) a Fluorine doped Tin Oxide (FTO) electrode had the photocatalyst deposited on it and served as the photoanode, (2) a platinum wire served as the counter electrode, and (3) a saturated calomel electrode (SCE) served as the reference electrode. For the fabrication of the photoanode, 50 mg of the sample was ground with 10 mg polyethylene glycol (PEG-6000) and 100 μL ethanol to make a slurry. Then, the slurry was coated onto a 1 cm \times 4 cm FTO electrode using a spin coating apparatus, and then allowed to dry in air. A 300 W xenon arc lamp ($\lambda \geq 420$ nm) (Perfect-light, PLS-SXE 300C, Beijing) was used as light source.

2.9. Photocatalytic HER experiments

Pt nanoparticles were photo-deposited on $\text{g-C}_3\text{N}_4$ samples in the 15 vol% triethanolamine (TEOA), 85% water containing a certain amount of H_2PtCl_6 using a full arc light ($\lambda > 300$ nm) for 2 h. Photocatalytic HER was performed at 5 °C which was cooled using a recirculated cooling water system. A 300 W xenon arc lamp was equipped with a 420 nm wavelength cutoff filter and had a light intensity of 120 $\text{mW}\cdot\text{cm}^{-2}$. Photocatalyst sample (25.0 mg) was dispersed in the TEOA solution (15 vol%, 80 mL) or deionized water only (80 mL, 18.2 $\text{M}\Omega$) for the water splitting experiments. The H_2 and O_2 was analyzed using gas chromatography (Shimadzu, GC2010), a 5 Å molecular sieve column (Plot-Q column, 0.32 μm) and high purity argon as carrier gas (99.999%).

3. Results and discussion

3.1. Photocatalyst characterization

The $\text{g-C}_3\text{N}_4$ samples were characterized by SEM, TEM, and scanning transmission electron microscope-high angle annular dark field (STEM-HAADF). The BCN agglomerated into bulk structure (inset, Fig. 1a), and the surface was smooth (Fig. 1a). After hydrothermal treatment, the OBCN had the same bulk feature with BCN (inset, Fig. 1b) although the surface became rough (Fig. 1b). In contrast, PCN showed a porous structure in the Fig. 1c due to steady NH_3 emission endowing porous formation under more sealed condensation condition (Fig. S1 and Table

S1, 2). After hydrothermal treatment, PCN was etched into sea-urchin morphology (Fig. 1d). The sea-urchin-structure formation should be attributed to the porous structure of PCN under hydrothermal condition. The X-ray energy dispersive spectra (EDS) showed that both BCN and OBCN displayed a weak O peak (Fig. 1e). The low peak intensity indicates low content of oxygen in the OBCN. In contrast, the CNSC exhibited a more obvious O peak (Fig. 1f). TEM images in the Fig. 1g and STEM-HAADF (Fig. 1h and inset, SAED) displayed amorphous sea-urchin structure of CNSC. The element mapping images confirmed the homogeneous distribution of C, N and O atoms in CNSC (Fig. 1i).

The BET surface area of CNSC was the highest among BCN, OBCN and PCN (Fig. S2 and Table S3). The large BET surface area can effectively absorb light and provide more sites for photocatalysis HER and OER. The X-ray diffraction (XRD) pattern showed the (100) facet at 13.0° and (002) facet at 27.7° (Fig. 2a), representing the inter-plane packing and inter-facial stacking. [41,42] As compared to BCN, (002) peak intensity decreased on other $\text{g-C}_3\text{N}_4$ (i.e., OBCN, PCN and CNSC) due to the reduction of crystallinity. [43,44] In the FT-IR spectra (Fig. 2b), the 810, 1200–1700 and 3200–3400 cm^{-1} peaks were ascribed to the tri-s-triazine ring out-of-plane bending, N=C=N heteroring and NH_2 stretching vibrations, respectively. [15–17] Both OBCN and CNSC showed a strong peak intensity at 3200–3400 cm^{-1} ascribed to the –OH groups. Moreover, CNSC displayed C=O characteristic peaks at 2720 and 1730 cm^{-1} in the Fig. 2c. Both PCN and CNSC showed C≡N characteristic peak at 2183 cm^{-1} (Fig. 2c and d), [26] not shown in the BCN and OBCN. Moreover, high-resolution X-ray photoelectron spectrum (XPS) N 1s spectra in the Fig. 2e indicated C≡N group was not created in the BCN and OBCN but formed in the PCN and CNSC at binding energy of 400.0 eV (Fig. 2f). [45]

To further investigate element composition and chemical bond covalent of the samples, both organic elemental analysis (OEA) and X-ray photoelectron spectroscopy (XPS) were performed. C, N, O and C/N atomic ratios determined by OEA were listed in Table S4. The O mol% of OBCN (4.45%) and CNSC (11.52%) were higher than for BCN (1.02%) and for PCN (1.38%), which was consistent with XPS survey record in the Fig. S3a. Moreover, the C/N ratio in PCN (0.75) was higher than BCN (0.67), which was due to the nitrogen defects in PCN. The high resolution XPS spectra of C 1s in the Fig. S3b indicated the basic unit of heptazine rings in the as-synthesized $\text{g-C}_3\text{N}_4$ samples. In the Fig. S3c, the XPS spectra of O 1s clearly presented CNSC had a OH peak at 531.56 eV and C=O peak at 533.15 eV. [46] The elemental analysis results were highly consistent with XPS analysis results (Table S5).

The UV-vis diffuse reflectance spectra (DRS) are shown in Fig. 3a. Compared to BCN and OBCN, PCN and CNSC showed absorption edge red shift to 700 nm, which was quite suitable for solar light utilization. In addition, the O doping (BCN vs. OBCN; PCN vs. CNSC) resulted in a blue shift of absorption edges. [36] The blue shifts should mainly be attributed to higher O 1s orbital energy than that of N 1s, which was consisting of VB [22,23]. The calculated bandgaps from Kubelka-Munk function for BCN, OBCN, PCN and CNSC were 2.68, 2.84, 1.63 and 2.07 eV, respectively (inset, Fig. 3a). The light absorption was visually reflected in the colour of the samples (inset, Fig. 3a). Obviously, the N-defect (C≡N) in the PCN and CNSC greatly narrowed the bandgaps. [25] And it displaced NH_2 groups at heptazine ring edges. [24–26] As shown in the Fig. 3b, VB potentials of BCN, OBCN, PCN and CNSC were +1.83, +1.98, +1.06 and 1.55 V vs. NHE, respectively, in the X-ray photoelectron spectrum-valence band (XPS-VB). According to band gap in the Fig. 3a. CB potentials of BCN, OBCN, PCN and CNSC were -0.83, -0.86, -0.57 and -0.52 V. vs. NHE. The VB values approximately agreed with the trend of the empirical formulas (Table S6). [46–48] Obviously, the O dopant in CNSC greatly changed the VB levels and enhances h^+ oxidation ability. [49]

Photoluminescence (PL) spectra can powerfully characterize the photoexcited charge separation in photocatalysts [50]. As shown in Fig. 3c, BCN and OBCN exhibited strong PL intensity, indicating fast

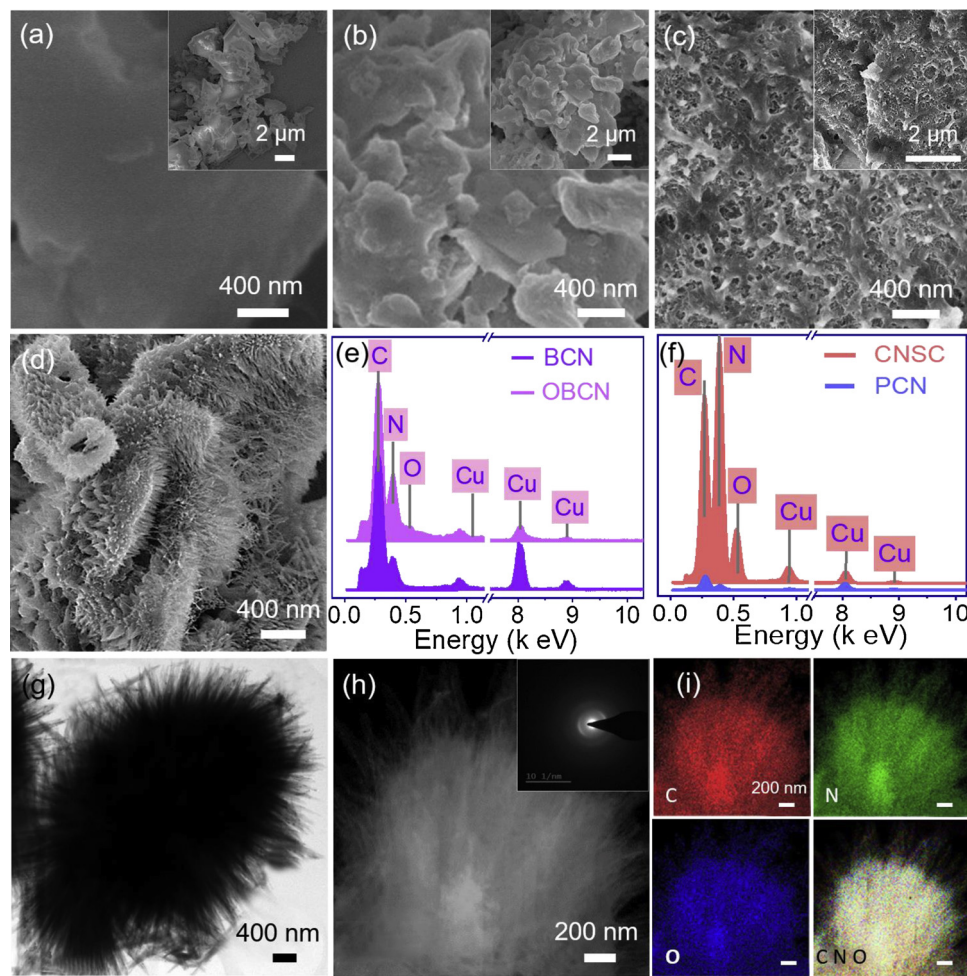


Fig. 1. SEM images of (a) BCN, (b) OBCN, (c) PCN, (d) CNSC, (e, f) EDS spectra of BCN, OBCN, PCN and CNSC, (g) TEM image of CNSC, (h) STEM-HADDF image of CNSC (inset, SAED) and (i) element mappings of CNSC.

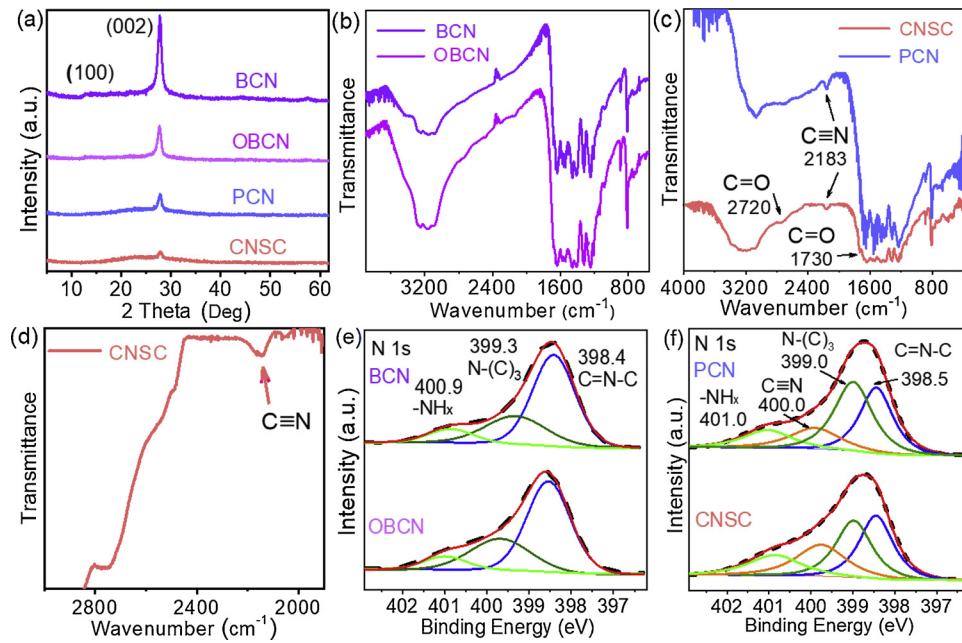


Fig. 2. (a) XRD patterns of BCN, OBCN, PCN and CNSC, (b) FT-IR spectra of BCN and OBCN, (c) FT-IR spectra of PCN and CNSC, (d) magnified FT-IR spectrum of CNSC, (e) high-resolution N 1s XPS of BCN and OBCN and (f) high-resolution N 1s XPS of PCN and CNSC.

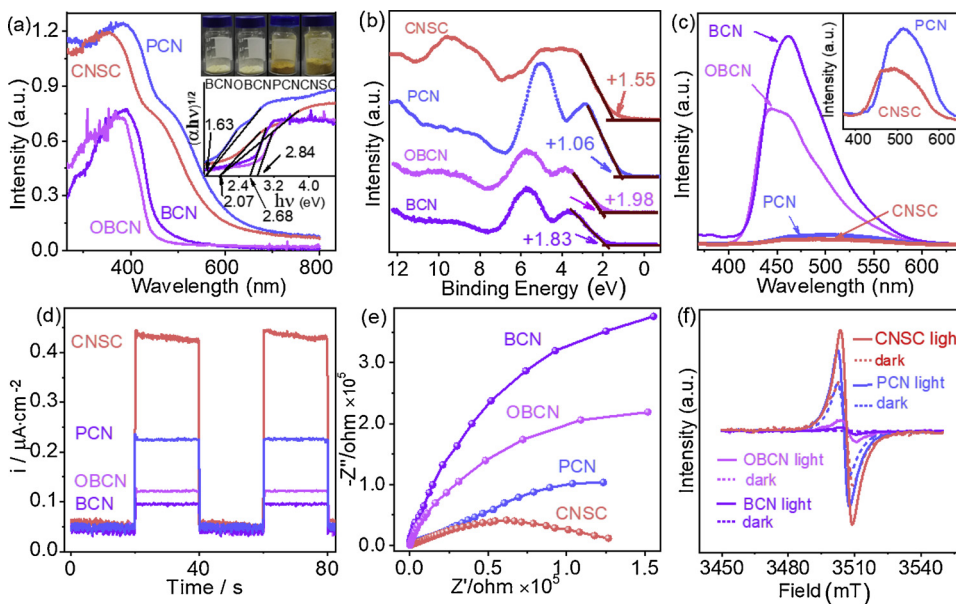


Fig. 3. (a) UV-vis DRS spectra (inset: Kubelka-Munk function and sample photograph), (b) XPS-VB, (c) PL spectra excited by 340 nm light under room temperature, (d) visible light photocurrent using 0.5 M Na_2SO_4 as supporting electrolyte ($\lambda \geq 420$ nm), (e) Nyquist plots and (f) EPR spectra of BCN, OBCN, PCN and CNSC under dark and visible light.

recombination of photogenerated charge. Comparatively, both PCN and CNSC showed negligible PL intensity, indicating rapid separation of photoinduced charge. [51] The photocurrent can also reflect the separation efficiency of photoinduced charge. [52] In Fig. 3d, CNSC showed the highest photocurrent density compared with other samples, implying the most efficient separation and transfer of photogenerated electrons. The fast electron transfer can be attributed to hierarchical sea-urchin nanostructure. Furthermore, CNSC had the smallest charge transfer resistance compared to BCN, OBCN and PCN (Fig. 3e). The electron paramagnetic resonance (EPR) signal ($g = 2.003$) is attributed to unpaired electrons in the π -conjugated aromatic rings of $\text{g-C}_3\text{N}_4$ [49–51]. As shown in Fig. 3f, the highest EPR signal intensity of CNSC indicated most delocalized electrons were excited and centralized on the CNSC, due to the $\text{C}\equiv\text{N}$, OH and $\text{C}=\text{O}$ groups with lone pair electrons. [52,53] Therefore, the unique sea-urchin nanomorphology of CNSC resulted in the most efficient separation and migration of charges among BCN, OBCN and PCN when photoexcited by visible light.

3.2. Computational chemistry results

Density functional theory (DFT) was performed to evaluate: (1) Pt stability on the $\text{g-C}_3\text{N}_4$ in the presence of $\text{C}\equiv\text{N}$, $\text{C}=\text{O}$ and OH groups, (2) projected density of states (PDOS) of Pt on the $\text{g-C}_3\text{N}_4$ and (3) d-band centers of Pt being deposited at $\text{g-C}_3\text{N}_4$ with varying numbers of $\text{C}\equiv\text{N}$, $\text{C}=\text{O}$ and OH groups. Fig. 4a showed that Pt can be photo-deposited on the CNSC and was stable without being affected by the $\text{C}\equiv\text{N}$, $\text{C}=\text{O}$ and OH groups. The PDOS of d-electrons of Pt showed that no matter with or without saturated OH , CN and $\text{C}=\text{O}$ groups (Fig. 4b–e), there were only slight differences shown in the PDOS distribution of d-electrons. This indicated that the overall electronic structures were not influenced by depositing Pt (Fig. S4). However, the calculated d-band centre (average energy of d-electrons) of Pt on $\text{g-C}_3\text{N}_4$ in the presence of OH , $\text{C}=\text{O}$ or $\text{C}\equiv\text{N}$ functional groups would generally shift positively as compared to when these functional groups are absent (Fig. 4f). Previously, Xu et al. [54] found that minor shifting the d-band centre of Pt closer to Fermi level could help to significantly enhance the photocatalytic hydrogen generation during water splitting on Pt deposited $\text{g-C}_3\text{N}_4$. According to the d-band theory that shifting of d-band centre towards Fermi level could lead to stabilization of adsorption; [55] and, in this case, OH , $\text{C}=\text{O}$ or $\text{C}\equiv\text{N}$ could help to provide sufficient driving force for hydrogen/oxygen evolution and benefit to redox reactions [56].

3.3. Photocatalytic performance

Impregnation with Pt plays an indispensable role because it forms a Schotke barrier prevent hole electron recombination and reactions sites for HER. Fig. S5a presented the HER of CNSC with different amount of Pt loadings under visible light ($\lambda \geq 420$ nm) using 15 vol% TEOA as electron donor. The optimal Pt loading amounts for BCN, OBCN, PCN and CNSC were 2 wt%, 2 wt%, 3 wt% and 3 wt% (Fig. S5a–d), respectively. As shown in Fig. S5e, 3 wt% Pt/CNSC had a HER of $3.45 \text{ mmol}\cdot\text{g}^{-1}\text{h}^{-1}$, which was 26.32, 9.60 and 2.43 times higher than 2 wt% Pt/BCN ($0.13 \text{ mmol}\cdot\text{g}^{-1}\text{h}^{-1}$), 2 wt% Pt/OBCN ($0.36 \text{ mmol}\cdot\text{g}^{-1}\text{h}^{-1}$) and 3 wt% Pt/PCN ($1.44 \text{ mmol}\cdot\text{g}^{-1}\text{h}^{-1}$) in the Fig. S5f respectively. Notably, apparent quantum efficiency (AQE) of 3 wt% Pt/CNSC reached as high as $32\% \pm 10 \text{ nm}$ (Fig. S5g), which was higher than most $\text{g-C}_3\text{N}_4$ -based photocatalysts (Table S7). After 60 h reaction, the HER performance of 3 wt% Pt/CNSC was still 95.3% of the original rate (Fig. S5h).

Also, water splitting was tested without TEOA under visible light irradiation. HER is negligible when Pt is not present (inset Fig. 5a and b). As shown in Fig. 5a and b, 3 wt% Pt/CNSC showed $41.5 \mu\text{mol}\cdot\text{g}^{-1}\text{h}^{-1}$ HER under visible light (AQE: $0.43\% \pm 10 \text{ nm}$), which was 30.3 and 11.2 times higher than 2 wt% Pt/BCN ($1.37 \mu\text{mol}\cdot\text{g}^{-1}\text{h}^{-1}$) and 2 wt% Pt/OBCN ($3.70 \mu\text{mol}\cdot\text{g}^{-1}\text{h}^{-1}$), respectively. In contrast, the HER of 3 wt% Pt/PCN was not observed, because h^+ had insufficient potential ($+1.06 \text{ V}$, Fig. 3b) to oxidize H_2O to form O_2 ($+1.23 \text{ V}$. vs. NHE). [57–59] Interestingly, H_2O_2 was detected in the water splitting reactions over 2 wt% Pt/BCN and 2 wt% Pt/OBCN, but not detected for 3 wt% Pt/CNSC (Fig. 5c). Approximately 0.28 and $3.12 \mu\text{M}$ H_2O_2 were collected in 60 min. during overall water splitting using 2 wt% Pt/BCN and 2 wt% Pt/OBCN, respectively (Fig. S6 and Fig. 5d). H_2O_2 will bind to the $\text{g-C}_3\text{N}_4$ and Pt, and hinder the overall water splitting. [60] Thus, the cyclic overall water splitting of 2 wt% Pt loaded BCN and OBCN displayed plateau (Fig. 5e), and was completely different from 3 wt% Pt/CNSC in Fig. 5f.

The results confirmed that the overall water splitting mechanism over 2 wt% Pt/BCN and 2 wt% Pt/OBCN involved both two-electron H_2O_2 evolution and four-electron O_2 production (Fig. 6a and b), and the VB holes for BCN and OBCN have oxidation potentials ($+1.83 \text{ V}$ for BCN and $+1.98 \text{ V}$ for OBCN). For 3 wt% Pt/PCN h^+ had insufficient potential ($+1.06 \text{ V}$) to oxidize H_2O into H_2O_2 and O_2 , and the overall water splitting reaction was hindered (Fig. 6c). With the proper VB potential, overall water splitting reaction occurred with 3 wt% Pt/CNSC

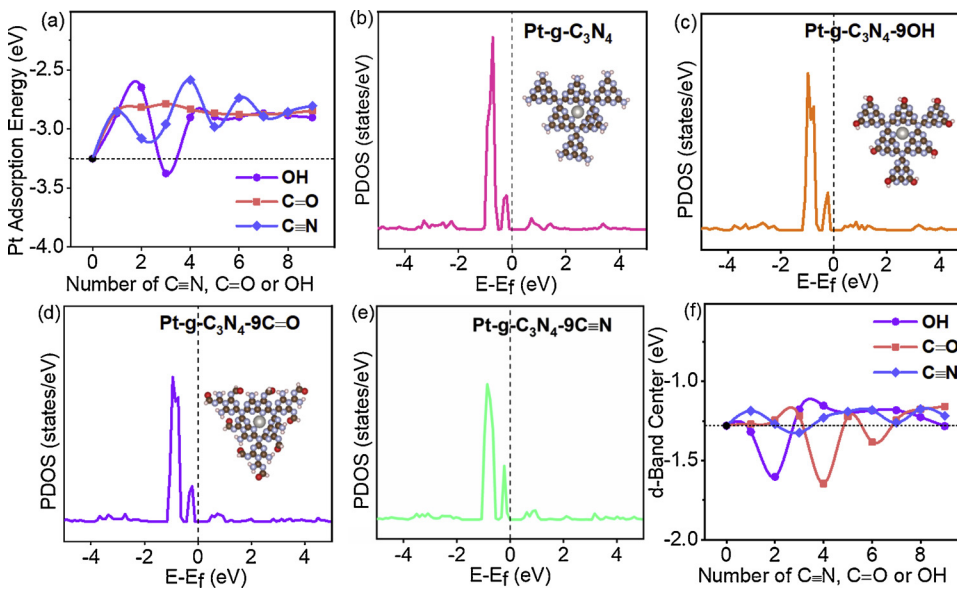


Fig. 4. (a) Calculated Pt stability at the $g\text{-C}_3\text{N}_4$ with varying numbers of $\text{C}\equiv\text{N}$, $\text{C}=\text{O}$ and OH . projected density of states (PDOS) of d-electrons of Pt being deposited at (b) $g\text{-C}_3\text{N}_4$ and the $g\text{-C}_3\text{N}_4$ with (c) OH , (d) $\text{C}=\text{O}$ and (e) $\text{C}\equiv\text{N}$ groups. The horizontal dashed lines represent the Fermi level. Insets showed the optimized structures. Blue, brown, pink, red and silver balls represent N, C, H, O, and Pt, respectively. More PDOS results can be found in the Figure S5. (f) Calculated d-band centre of Pt deposited at $g\text{-C}_3\text{N}_4$ with varying numbers of $\text{C}\equiv\text{N}$, $\text{C}=\text{O}$ and OH groups. Fermi energy (E_f) is used as the references of d-band energies (For interpretation of the references to colour in this figure legend, the reader is referred to the web version of this article).

through a four-electron H_2O oxidation process, and produced H_2 and O_2 (Fig. 6d).

The thermal stability is indispensable when used in practical applications.

CNSC had good stability without collapse when it was exposed to air at 300 °C overnight, and still had the “sea-urchin” nanostructure (Figure S7a). After the same thermal treatment, the HER for 3 wt% Pt/CNSC was $4.13 \text{ mmol}\cdot\text{g}^{-1}\text{h}^{-1}$ using the 15 vol% TEOA and visible light ($\lambda \geq 420 \text{ nm}$) (Figure S7b). In addition, CNSC still remained the unique hierarchical sea-urchin nanostructure after 60 h (Figure S7c). The C, N and O atom content in the CNSC remained the same and this was confirmed by EDS analysis (Figure S7d and Table S8).

The remarkable photocatalytic performance of CNSC was attributed to the following factors: (1) unique sea-urchin nanostructure efficiently promoted photoinduced $h^+ - e^-$ pairs separation and exposed more reactive sites; (2) the nitrogen vacancies in the CNSC narrowed down the bandgap with more visible light utilization; and, (3) band structure (bandgap of 2.07 eV, VB of +1.55 V for OER, and CB of -0.52 V for HER) was highly favorable for thermodynamic overall water splitting reactions and does not have a significant over potential which prevents the production of H_2O_2 from the oxidation of water (ca. +1.8 V vs.

NHE). On the basis of charge migration in the CNSC, the photo-excited electrons in the CB migrated to VB, and then transferred to Pt for HER, while the holes in VB for H_2O oxidation OER. As a result, the unique sea-urchin-like morphology and band structure promoted water splitting reaction over 3 wt% Pt/CNSC.

4. Conclusion

A hierarchical sea-urchin-structure CNSC with a small bandgap (~2.0 eV) was synthesized using sealed condensation approach. DFT calculations confirmed that OH, $\text{C}=\text{O}$, and $\text{C}\equiv\text{N}$ groups could tune the d-band centers of Pt atoms, leading to higher catalytic performance and better stabilization of adsorbate. 3 wt% Pt/CNSC showed 41.5 and $20.3 \text{ }\mu\text{mol}\cdot\text{g}^{-1}\text{h}^{-1}$ for HER and OER in the overall water splitting under visible light ($\lambda \geq 420 \text{ nm}$), respectively. And HER of 3 wt% Pt/CNSC photocatalyst had 30 times greater HER than the 2 wt% Pt/BCN. The CNSC has more wide visible light absorption range (~2.0 eV bandgap) and a sea-urchin nanostructure. And it paves a pathway for developing high-performance $g\text{-C}_3\text{N}_4$ -based photocatalysts for solar light conversion to hydrogen fuel.

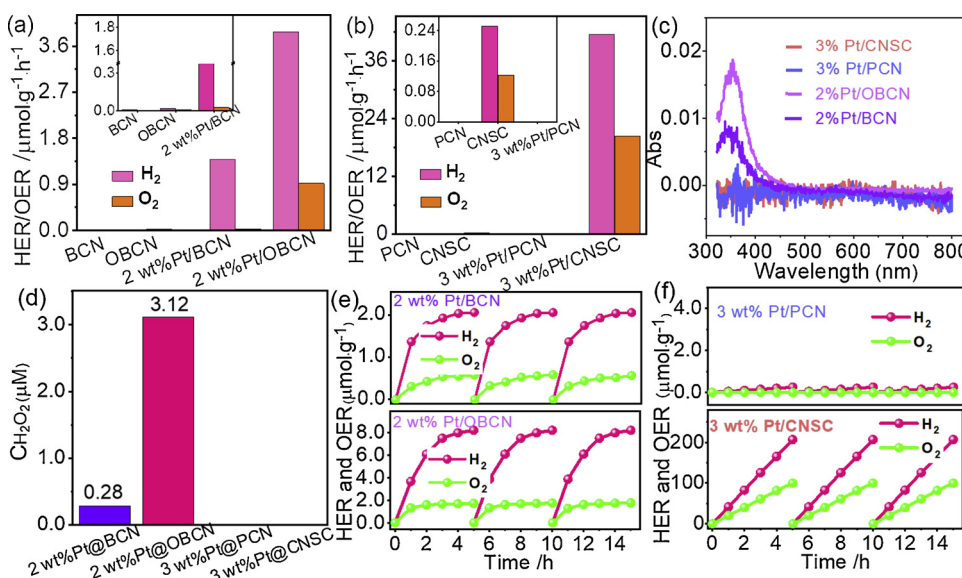


Fig. 5. (a) Overall water splitting of BCN, 2 wt % Pt/BCN, OBCN and 2 wt% Pt/OBCN, the inset in (a) showed the overall water splitting of BCN, OBCN and 2 wt% Pt/BCN, (b) overall water splitting of PCN, 3 wt% Pt/PCN, CNSC and 3 wt% Pt/CNSC, the inset in (b) showed the overall water splitting of PCN, CNSC and 3 wt% Pt/PCN, (c) H_2O_2 detection by UV-vis spectroscopy, (d) H_2O_2 evolution in the overall water splitting of 2 wt% Pt/BCN, 2 wt% Pt/OBCN, 3 wt% Pt/PCN and 3 wt% Pt/PCN, (e) cyclic overall water splitting of 2 wt% Pt/BCN and 2 wt% Pt/OBCN and (f) cyclic overall water splitting of 3 wt% Pt/PCN and 3 wt% Pt/CNSC. Reaction conditions: (a-f) purified water overall splitting without TEOA under visible light ($\lambda \geq 420 \text{ nm}$), every 5 h as a period by recovering the catalyst and started with fresh purified water.

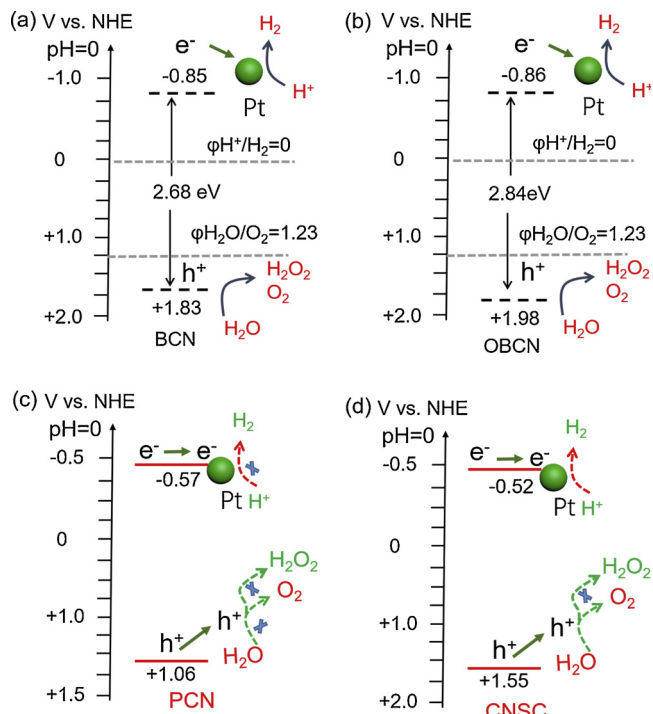


Fig. 6. (a) Bandgap structures and visible-light photocatalysis overall water splitting HER and OER mechanisms of (a) 2 wt% Pt/BCN, (b) 2 wt% Pt/OBCN, (c) 3 wt% Pt/PCN and (d) 3 wt% Pt/CNSC.

Acknowledgements

This work was supported by the National Natural Science Foundation of China (51778218 and 51478171) and Hunan Provincial Innovation Foundation for Postgraduate (CX2017B139 and CX2017B141). The authors appreciate the support from the Brook Byers Institute for Sustainable Systems, Hightower Chair and the Georgia Research Alliance at Georgia Institute of Technology. The views and ideas expressed herein are solely those of the authors and do not represent the ideas of the funding agencies in any form.

Appendix A. Supplementary data

Supplementary material related to this article can be found, in the online version, at doi:<https://doi.org/10.1016/j.apcatb.2019.03.010>.

References

- Y. Wu, P. Wang, X. Zhu, Q. Zhang, Z. Wang, Y. Liu, G. Zou, Y. Dai, M.H. Whangbo, B. Huang, *Adv. Mater.* 30 (2018) 1704342.
- S. Chu, Y. Cui, N. Liu, Y. Wang, X. Wang, M. Antonietti, *Angew. Chem. Int. Ed.* 51 (2012) 68–89.
- D. Voiry, H.S. Shin, K. Ping, M. Chhowalla, *Nat. Rev. Chem.* 2 (2018) 0105.
- S. Gao, Z. Zhang, K. Liu, B. Dong, *Appl. Catal. B-Environ.* 188 (2016) 245–252.
- A.M. Beiler, G.F. Moore, *Nat. Chem.* 10 (2018) 3–4.
- L. Kornblum, D.P. Fenning, J. Faucher, J. Hwang, A. Boni, M.G. Han, M.D. Morales-Acosta, Y. Zhu, E.I. Altman, M.L. Lee, C.H. Ahn, F.J. Walker, Y. Shao-Horn, *Energy Environ. Sci.* 10 (2017) 377–382.
- S. Docao, A.R. Koirala, M.G. Kim, I.C. Hwang, M.K. Song, K.B. Yoon, *Energy Environ. Sci.* 10 (2017) 628–640.
- C. Han, M.Q. Yang, B. Weng, Y.J. Xu, *Phys. Chem. Chem. Phys.* 16 (2014) 16891–16903.
- Y. Zhang, Z. Chen, S. Liu, Y.J. Xu, *Appl. Catal. B-Environ.* 140–141 (2013) 598–607.
- W. Jiang, Y. Liu, R. Zong, Z. Li, W. Yao, Y. Zhu, *J. Mater. Chem. A* 3 (2015) 18406–18412.
- J. Zhang, M. Zhang, R.Q. Sun, X. Wang, *Angew. Chem. Int. Ed.* 51 (2012) 10145–10149.
- G. Zhang, C. Huang, X. Wang, *Small* 11 (2015) 1215–1221.
- J. Li, Y. Zhang, X. Zhang, J. Han, Y. Wang, L. Gu, Z. Zhang, X. Wang, J. Jian, P. Xu, B. Song, *ACS Appl. Mater. Interfaces* 7 (2015) 19626–19634.
- Z. Chen, T.T. Fan, X. Yu, Q.L. Wu, Q.H. Zhu, L.Z. Zhang, J.H. Li, W.P. Fang, X.D. Yi, *J. Mater. Chem. A* 6 (2018) 15310–15319.
- J. Barrio, L. Lin, X. Wang, M. Shalom, *ACS Sustain. Chem. Eng.* (6) (2018) 519–530.
- M. Shalom, M. Guttentag, C. Fettkenhauer, S. Inal, D. Neher, A. Llobet, M. Antonietti, *Chem. Mater.* 26 (2014) 5812–5818.
- X. Wang, K. Maeda, A. Thomas, K. Takanabe, G. Xin, J.M. Carlsson, K. Domen, M. Antonietti, *Nat. Mater.* 8 (2009) 76–80.
- Z. Tong, D. Yang, Z. Li, Y. Nan, F. Ding, Y. Shen, Z. Jiang, *ACS Nano* 11 (2017) 1103–1112.
- J.N. Tiwari, Y.K. Seo, T. Yoon, W.G. Lee, W.J. Cho, M. Yousuf, A.M. Harzandi, D.S. Kang, K.Y. Kim, P.G. Suh, K.S. Kim, *ACS Nano* 11 (2017) 742–751.
- Q. Han, Z. Cheng, B. Wang, H. Zhang, L. Qu, *ACS Nano* 12 (2018) 5221–5227.
- P. Niu, G. Liu, H.M. Cheng, *J. Phys. Chem. C* 116 (116) (2012) 11013–11018.
- S.W. Boettcher, E.L. Warren, M.C. Putnam, E.A. Santori, D. Turner-Evans, M.D. Kelzenberg, M.G. Walter, J.R. McKone, B.S. Brunschwig, H.A. Atwater, N.S. Lewis, *J. Am. Chem. Soc.* 133 (2011) 1216–1219.
- E. Tunkara, C. Albayrak, E.O. Polat, C. Kocabas, Ö. Dag, *ACS Nano* 8 (2014) 11007–11012.
- P. Niu, L.C. Yin, Y.Q. Yang, G. Liu, H.M. Cheng, *Adv. Mater.* 26 (2014) 8046–8052.
- G. Liu, G. Zhao, W. Zhou, Y. Liu, H. Pang, H. Zhang, D. Hao, X. Meng, P. Li, T. Kako, J. Ye, *Adv. Funct. Mater.* 26 (2016) 6822–6829.
- Y. Kang, Y. Yang, L.C. Yin, X. Kang, G. Liu, H.M. Cheng, *Adv. Mater.* 27 (2015) 4572–4577.
- J. Barrio, L. Lin, P. Amo-Ochoa, J. Tzadikov, G. Peng, J. Sun, F. Zamora, X. Wang, M. Shalom, *Small* 14 (2018) 1800633.
- J. Yuan, X. Liu, Y. Tang, Y. Zeng, L. Wang, S. Zhang, T. Cai, Y. Liu, S. Luo, Y. Pei, C. Liu, *Appl. Catal. B-Environ.* 237 (2018) 24–31.
- V.W. Liu, I. Moudrakovski, T. Botari, S. Weinberger, M.B. Mesch, V. Duppel, J. Senker, V. Blum, B.V. Lotsch, *Nat. Commun.* 7 (2016) 12165.
- J. Fu, B. Zhu, C. Jiang, B. Cheng, W. You, J. Yu, *Small* 13 (2017) 1603938.
- J. Li, Q. Pei, R. Wang, Y. Zhou, Z. Zhang, Q. Cao, D. Wang, W. Mi, Y. Du, *ACS Nano* 12 (2018) 3351–3359.
- Y. Qu, X. Duan, *Chem. Soc. Rev.* 42 (2013) 2568–2580.
- W. Tu, Y. Xu, J. Wang, B. Zhang, T. Zhou, S. Yin, S. Wu, C. Li, Y. Huang, Y. Zhou, Z. Zou, J. Robertson, M. Kraft, R. Xu, *ACS Sustain. Chem. Eng.* 5 (2017) 7260–7268.
- P. Li, Y. Zhou, Z. Zhao, Q. Xu, X. Wang, M. Xiao, Z. Zou, *J. Am. Chem. Soc.* 137 (2015) 9547–9550.
- M. Zhu, Z. Sun, M. Fujitsuka, T. Majima, *Angew. Chem. Int. Ed.* 57 (2018) 2160–2164.
- Y. Zeng, C. Liu, L. Wang, S. Zhang, Y. Ding, Y. Xu, Y. Liu, S. Luo, *J. Mater. Chem. A* 4 (2016) 19003–19010.
- W. Che, W. Cheng, T. Yao, F. Tang, W. Liu, H. Su, Y. Huang, Q. Liu, J. Liu, F. Hu, Z. Pan, Z. Sun, S. Wei, *J. Am. Chem. Soc.* 139 (2017) 3021–3026.
- Y. Zheng, Y. Jiao, Y. Zhu, Q. Cai, A. Vasileff, L.H. Li, Y. Han, Y. Chen, S.Z. Qiao, *J. Am. Chem. Soc.* 139 (2017) 3336–3339.
- W. Xing, C. Li, G. Chen, Z. Han, Y. Zhou, Y. Hu, Q. Meng, *Appl. Catal. B-Environ.* 203 (2017) 65–71.
- X. Yang, Z. Chen, J. Xu, H. Tang, K. Chen, Y. Jiang, *ACS Appl. Mater. Interfaces* 7 (2015) 15285–15293.
- T.Y. Ma, Y. Tang, S. Dai, S.Z. Qiao, *Small* 10 (2014) 2382–2389.
- F. He, G. Chen, J. Miao, Z. Wang, D. Su, S. Liu, W. Cai, L. Zhang, S. Hao, B. Liu, *ACS Energy Lett.* 1 (2016) 969–975.
- X. Zhang, X. Xie, H. Wang, J. Zhang, B. Pan, Y. Xie, *J. Am. Chem. Soc.* 135 (2013) 18–21.
- J. Tian, Q. Liu, A.M. Asiri, A.O. Al-Youbi, X. Sun, *Anal. Chem.* 85 (2013) 5595–5595.
- H. Kiuchi, R. Shibuya, T. Kondo, J. Nakamura, H. Niwa, J. Miyawaki, M. Kawai, M. Oshima, Y. Harada, *Nanoscale Res. Lett.* 11 (2016) 127–133.
- D. Jiang, J. Zhu, M. Chen, J. Xie, *J. Colloid Interface Sci.* 417 (2014) 115.
- P. Suyana, P. Ganguly, B.N. Nair, A.P. Mohamed, K. Warrier, U. Hareesh, *Environ. Sci. Nano* 4 (2017) 212.
- P. Suyana, K. Sneha, B.N. Nair, V. Karunakaran, A.P. Mohamed, K. Warrier, U. Hareesh, *RSC Adv.* 6 (2016) 17800.
- C.F. Tan, A. Kyi, S.S. Zin, Z. Chen, C.H. Liow, H.T. Phan, H.R. Tan, Q.H. Xu, G.W. Ho, *ACS Nano* 12 (2018) 4512–4520.
- Y. Zeng, X. Liu, B. Liu, L. Wang, Y. Xia, S. Zhang, S. Luo, Y. Pei, *Appl. Catal. B-Environ.* 224 (2018) 1–9.
- C.F. Tan, A. Kyi, S.S. Zin, Z. Chen, C.H. Liow, H.T. Phan, H.R. Tan, Q.H. Xu, G.W. Ho, *ACS Nano* 12 (2018) 4512–4520.
- L. Yang, J. Huang, L. Yang, J. Huang, L. Shi, L. Cao, Q. Yu, Y. Jie, J. Fei, H. Ouyang, J. Ye, *Appl. Catal. B-Environ.* 204 (2017) 335–345.
- J. Zhang, G. Zhang, X. Chen, S. Lin, L. Möhlmann, G. Dolega, G. Lipner, M. Antonietti, S. Blechert, X. Wang, *Angew. Chem. Int. Ed.* 51 (2012) 3183–3187.
- Y. Chen, B. Wang, S. Lin, Y. Zhang, X. Wang, *J. Phys. Chem. C* 118 (2014) 29981–29989.
- Z. Xu, M.G. Kibria, B. AlOtaibi, P.N. Duchesne, L.V. Besteiro, Y. Gao, Q. Zhang, Z. Mi, P. Zhang, A.Q. Govorov, L. Mai, M. Chaker, D. Ma, *Appl. Catal. B-Environ.* 77 (2018) 77–85.
- J.K. Nørskov, F. Abild-Pedersen, F. Studt, T. Bligaard, *Proc. Natl. Acad. Sci. U. S. A* 108 (2011) 937–943.
- H. Li, G. Henkelman, *J. Phys. Chem. C* 121 (2017) 27504–27510.
- H. Pan, T. Takata, K. Domen, *Chem. Eur. J.* 22 (2016) 1854–1862.
- K. Zhang, L. Wang, X. Sheng, M. Ma, M.S. Jung, W. Kim, H. Lee, J.H. Park, *Adv. Energy Mater.* 6 (2016) 1502352.
- Y. Shiraishi, S. Kanazawa, Y. Sugano, D. Tsukamoto, H. Sakamoto, S. Ichikawa, T. Hirai, *ACS Catal.* 14 (2014) 774–780.